The Journal of the Astronautical Sciences (2026) 73:94
https://doi.org/10.1007/s40295-026-00639-2

RESEARCH

Design and Analysis of the Transfer Trajectory for the LUMIO Cislunar CubeSat Mission

Carmine Giordano[1] · Alessandro Martinelli[1] · Carmine Buonagura[1] · Gianmario Merisio[1] · Vittorio Franzese[1] · Francesco Topputo[1]

Received: 4 April 2025 / Accepted: 8 September 2026
© The Author(s) 2026

Abstract

The Earth–Moon system is constantly impacted by Solar System meteoroids causing threats to space and ground assets. A detailed characterization of meteoroid impact magnitudes, velocities, and distribution in time and space is fundamental for a proper space threats assessment and mitigation. The lunar surface is a natural detector of such impact phenomena. The LUMIO CubeSat mission aims to observe and characterize meteoroid impacts on the lunar farside, enhancing lunar situational awareness and complementing Earth-based observations of the lunar near-side. This study presents the mission design and analysis of LUMIO's transfer trajectory, which exploits weak stability boundary dynamics to achieve a cost-effective insertion into the target halo orbit. Leveraging weak stability boundaries reduces the required spacecraft propellant and increases the number of launch opportunities. While focusing on the specific LUMIO mission, this work also highlights key features of the weak stability boundary transfer design which might prove useful for future cislunar missions, and especially for miniaturized platforms.

Keywords Mission analysis · CubeSat mission · Trajectory design and optimization · Weak stability boundaries · LUMIO · Cislunar environment

✉ Carmine Giordano
carmine.giordano@polimi.it

Alessandro Martinelli
alessandro2.martinelli@polimi.it

Carmine Buonagura
carmine.buonagura@polimi.it

Gianmario Merisio
gianmario.merisio@polimi.it

Vittorio Franzese
vittorio.franzese@polimi.it

Francesco Topputo
francesco.topputo@polimi.it

[1] Department of Aerospace Science and Technology, Politecnico di Milano, Via La Masa, 34, 20156 Milan, Italy

Published online: 19 October 2026

1 Introduction

The Earth–Moon environment is continually struck by meteoroids, remnants of asteroidal and cometary debris dating to the early Solar System, that produce impact flashes upon collision [1]. Decades of terrestrial meteor-shower observations have underpinned the development of comprehensive meteoroid flux models, which forecast micrometeoroid erosion of spacecraft and assess potential large-body impact hazards to Earth. By extending these models through lunar impact monitoring, where the flux closely mirrors that at Earth, it becomes possible to extract detailed distributions of impactor sizes, velocities, and temporal-spatial occurrence. Such information not only refines existing meteoroid environment models and validates lunar impact simulations, but also informs lunar seismology, interior-structure modeling, and future situational-awareness systems for crewed and robotic missions [2].

Ground-based telescopes have long captured the transient flashes from meteoroid strikes on the Moon, providing critical data to verify and improve both Earth-orbit and cislunar meteoroid models [3]. Monitoring from Earth benefits from wide fields of view but is constrained by weather, lunar phase, and geometric visibility, limiting both the duration and smallest detectable impactors [4]. Positioning an optical sensor in the lunar vicinity can increase detection rates and extend sensitivity down to sub-millimeter particles thanks to the reduced viewing distance [2, 5]. In particular, an Earth–Moon L_2 halo orbit enables continuous surveillance of the lunar far side.

The Lunar Meteoroid Impacts Observer (LUMIO) was conceived under ESA's SysNova competition "LUnar CubeSats for Exploration (LUCE)" to capitalize on these advantages. Selected alongside three other studies in 2019 and winning the challenge ex-aequo, LUMIO's goal is to quantify and characterize impact flashes on the lunar far side, augmenting Earth-based surveys [2]. Phase A confirmed feasibility through mission definition review (MDR) in July 2020 and preliminary requirements review (PRR) in February 2021, with results detailed in [6]. The Phase B of the mission, funded by the European Space Agency (ESA) under the General Support Technology Programme (GSTP), through the support of the Italian Space Agency (ASI) and Norway Space Agency (NOSA), ran from September 2022 through October 2023, advancing the mission design toward implementation.

The LUMIO platform is constituted by a 12U-XL CubeSat. The spacecraft is equipped with the LUMIO-Cam, an optical instrument capable of detecting light flashes in the visible and near-infrared spectrum to continuously monitor and process the data [7].

The LUMIO mission has been devised to address the following issues:

- **Science Question**. What are the spatial and temporal characteristics of meteoroids impacting the lunar surface?
- **Science Goal**. To advance the understanding of how meteoroids evolve in the cislunar space by observing the flashes produced by their impacts on the lunar surface.
- **Science Objective**. To characterize the flux of meteoroids impacting the lunar surface.

LUMIO shall also validate some European miniaturized technologies for the lunar environment such as a novel propulsion system, as well as advanced CubeSat navigation and control capabilities [8], contributing to the growing body of evidence that CubeSats can serve as viable platforms for deep-space science and exploration.

Throughout its design, LUMIO nominal operational orbit has been a halo orbit around the Earth–Moon L_2 point, chosen for uninterrupted far-side visibility and minimal station-keeping requirements [9]. On the other hand, to account for rideshare opportunities, alternative deployment options (e.g., insertion into a high-elliptical lunar orbit [10] or an Artemis-like transfer [11]) were evaluated during the project. Given the growing use of solar-perturbed weak stability boundary (WSB) transfers to the Moon, where third-body effects are leveraged to enable low-Δv lunar arrival and (often) ballistic capture, missions such as KPLO, CAPSTONE, and Hakuto-R have demonstrated the feasibility of this cost-effective transfer approach [12–15]. Recent studies have also investigated low-energy lunar transfers specifically tailored to secondary payloads, showing how rideshare constraints and limited control authority can be addressed through multi-phase trajectory design, lunar passages, and dynamical-systems-based construction strategies [16, 17]. Consequently, LUMIO adopted WSB as its preferred Phase B transfer strategy, balancing propellant efficiency and flexibility needed by small satellites for lunar insertion.

This work details the mission design and analysis of the LUMIO CubeSat, as outcome of its Phase B study, with a particular focus to the new nominal transfer exploiting WSB.

The paper is organized as follows: Sects. 2 and 3 present the mission design and analysis, respectively, with results provided in Sect. 4. Lastly, Sect. 5 summarizes and concludes the present work.

2 Mission Design

2.1 Background

The selection of the LUMIO operational orbit was consolidated during the Phase 0 design through a multi-level trade-off analysis [9]. The process first identified the orbit families compatible with lunar farside monitoring, mission lifetime, and accessibility constraints, and then compared the feasible candidates in terms of science return and operational cost. The main acceptance drivers were the capability to observe impact flashes on the lunar farside at night, to detect meteoroid impacts within the required kinetic-energy range, to guarantee at least one year of operations, and to remain compatible with the CubeSat Δv budget. The main selection drivers were instead the maximization of the expected number of detectable meteoroid impacts, the minimization of transfer and station-keeping cost, and the availability of lunar full-disk viewing opportunities for optical navigation.

The preliminary trade-off considered both selenocentric orbits and libration-point orbits, including low-lunar orbits, frozen orbits, halo orbits, distant retrograde orbits, and low prograde orbits. Frozen orbits were discarded by the coverage analysis because they did not satisfy the meteoroid-detection requirements over the required kinetic-

Table 1 Parameters of three-body halo generating the selected operational orbit

Name	C_j (adim)	A_z (km)
Halo_Cj3p09	3.09	28,418.41

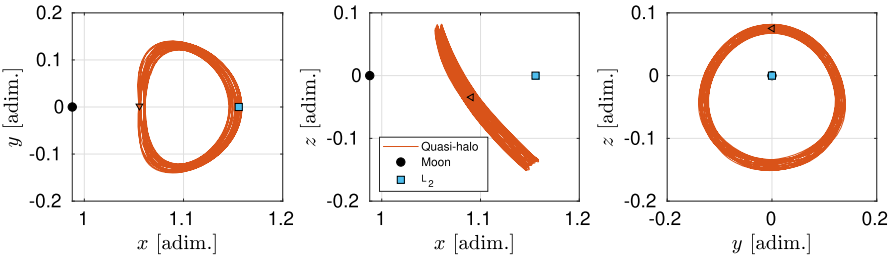


Fig. 1 Example of the operational Earth–Moon L_2 high-fidelity quasi-halo in the roto-pulsating synodic frame introduced in Sect. 3.1

energy range, whereas Earth–Moon L_2 halo and vertical Lyapunov orbits satisfied the science-related acceptance criteria. The halo family was finally selected because it provided a favorable compromise between lunar farside visibility, continuous spacecraft visibility from Earth, reduced eclipse occurrences, transfer accessibility, and station-keeping cost. Within this family, the halo orbit with Jacobi constant $C_j = 3.09$ was selected because it lies in a broad minimum of the total maneuver-cost trade-off, providing both low transfer cost and robustness with respect to errors in the injected stable-manifold energy level. The selected solution is a quasi-periodic orbit about the Earth–Moon L_2 point, hereafter referred to as quasi-halo orbit. This orbit is generated from a circular restricted three-body problem halo orbit with Jacobi constant $C_j = 3.09$ and subsequently propagated in the high-fidelity n-body dynamics introduced in Sect. 3.1.

Table 1 reports the nondimensional Jacobi constant and the out-of-plane amplitude A_z of the generating three-body halo orbit. An example of a corresponding quasi-halo orbit, represented in the roto-pulsating frame, is shown in Fig. 1.

Contrary to the selection of the operational orbit, the strategy for the transfer trajectory and possible release conditions has been changed several times during the project, according to the launch availability and the technical limitation related to the CubeSat. Specifically, during the Phase 0 study, LUMIO was supposed to be released by the Lunar Service Pathfinder into a 200 × 15,000 km low-Lunar orbit (LLO). The Lunar Service Pathfinder was a spacecraft by Surrey Satellite Technology Ltd in collaboration with the European Space Agency.[1] From this release orbit, LUMIO would then independently reach its final orbit by exploiting the quasi-halo manifolds [9]. During the ESA Concurrent Design Facility study, the orbit was changed to a 600 × 20,000 km altitude orbit to reduce the magnitude of the stable-manifold-injection maneuver (SMIM). Further studies developed during Phase B assessed that this kind of injection orbit was unsuitable for a number of reasons, such as the elevated Δv

[1] See https://www.esa.int/ESA_Multimedia/Images/2024/10/Lunar_Pathfinder_for_lunar_connection. Last accessed on March 1, 2025.

costs, not compatible with the platform, the high magnitude of the SMIM, and the single point failure of the maneuver that could have jeopardized the mission.

Recently, a number of space missions have taken advantage of the weak stability boundary to travel from Earth to the Moon by exploiting the Sun gravitational influence to drift toward the lunar region without expending extra fuel. In the near future, opportunities to reach the Moon in this fashion may be provided through the Commercial Lunar Payload Services (CLPS). The CLPS is a program launched by NASA to send robotic probes and rovers on the lunar surface with the primary goal of studying lunar resources, testing in-situ resource utilization, and performing science investigation to deepen the lunar environment knowledge to support the Artemis program.[2] CLPS will provide end-to-end services from the Earth to the lunar surface. As of February 2025, NASA already contracted 8 missions, hosting more than 25 payloads, with the first launch that took place in January 2024. Several others flight opportunities are scheduled in the near future. Some of these trajectories involve a WSB transfer to reach a LLO.

During Phase B, a WSB transfer emerged as an appealing option for LUMIO. This choice was driven by the potential propellant savings to reach the operational orbit and by the prospect of multiple near-term carrier spacecraft capable of deploying CubeSats onto similar transfer trajectories.

2.2 WSB Opportunity

The WSB opportunity has been analyzed to understand the advantages and drawbacks it would introduce to the mission. Table 2 summarizes the pros and cons related to a weak stability boundary transfer.

The main advantage is the significant reduction in the transfer Δv budget. This reduction implies smaller propellant and pressurant tanks, leading to an increase in available spacecraft volume. This increased volume has significant implications from both a scientific and operational perspective. Savings in tanks volume allow for a longer baffle of the optical payload and provides more internal space for components, such as the payload proximity electronics. Additionally, the use of WSB eliminates some constraints from Phase A, such as the need for a 16U deployer to release the spacecraft and allows for the reintroduction of the second star-tracker, which had been removed due to space constraints. Regarding operations, LUMIO will undergo a comparatively low-intensity commissioning phase lasting only a few days early in the mission, and the longer transfer duration allows more flexible operations thereafter. However, there are two main drawbacks associated with this transfer. First, the spacecraft reaches a high-Earth distance, making the closure of the link-budget analysis more challenging. Second, the extended transfer time may result in higher operational costs.

WSB transfers enable both a dedicated launch (e.g., CAPSTONE [14]) and rideshare opportunities (e.g., HAKUTO-R with Lunar Flashlight [18]). However, dedicated and piggyback launch opportunities yield significantly different outcomes. A dedicated launch would release LUMIO directly onto the desired translunar trajectory, targeting the halo orbit at the specified epoch. This approach offers the advantage of

[2] See https://www.nasa.gov/commercial-lunar-payload-services/. Last accessed on March 1, 2025.

Table 2 Advantages and drawbacks of the WSB transfer

Advantages	Drawbacks
Lower Δv involving smaller tanks	Higher distance from the Earth (up to 2×10^6 km)
Extended commissioning phase	Longer transfer time (up to 150 days)
Less frequent operations	–
Both piggyback and a dedicated launch	–
Use of a smaller deployer	–

reduced deterministic maneuver costs but at the expense of higher launch costs. In contrast, a piggyback launch significantly reduces launch costs because LUMIO serves as the secondary payload on a launcher, necessitating alignment with the primary payload mission objectives. Under this arrangement, LUMIO would still be placed on a trans-lunar trajectory, but flexibility is limited regarding the departure date and the final orbit of the transfer trajectory. Consequently, LUMIO would need to perform deep-space maneuvers to reach the desired halo orbit, resulting in a significant increase in deterministic maneuvering costs.

As a result, given the uncertainty surrounding the type of launch opportunity LUMIO will encounter, LUMIO is considered to be released along the WSB transfer by a primary mission (e.g., a CLPS mission), representing the worst-case scenario in terms of mission flexibility and deterministic maneuvers cost. For the rideshare (worst-case) scenario, we assume the carrier spacecraft proceeds to a LLO, consistent with CLPS-like lunar delivery missions; LUMIO then retargets from the release point to its Earth–Moon L_2 operational orbit. Once released in Earth proximity, LUMIO will use its own thruster to target the halo orbit about Earth–Moon L_2. It is important to note that this scenario would embrace not only a shared launch, but also the possibility to exploit a dedicated launch. A summary of the final mission design is presented in Fig. 2.

3 Trajectory Design

In the Phase B scenario, LUMIO is released from its carrier spacecraft during the Sun–Earth WSB transfer (for example, as a payload on a CLPS mission). The primary vehicle proceeds into low-lunar orbit and performs its own orbit-insertion maneuver, while LUMIO independently moves from the release point to its designated quasi-halo orbit around the Earth–Moon L_2 point. Consequently, the overall mission path can be divided into two distinct layers (see Fig. 3):

Layer 1 The trajectory followed by the mothercraft. After a kick provided by the launcher in low Earth orbit (LEO), the mothercraft follows a WSB transfer to the Moon, enters the LLO via a targeted insertion burn, and stabilizes itself in lunar orbit.

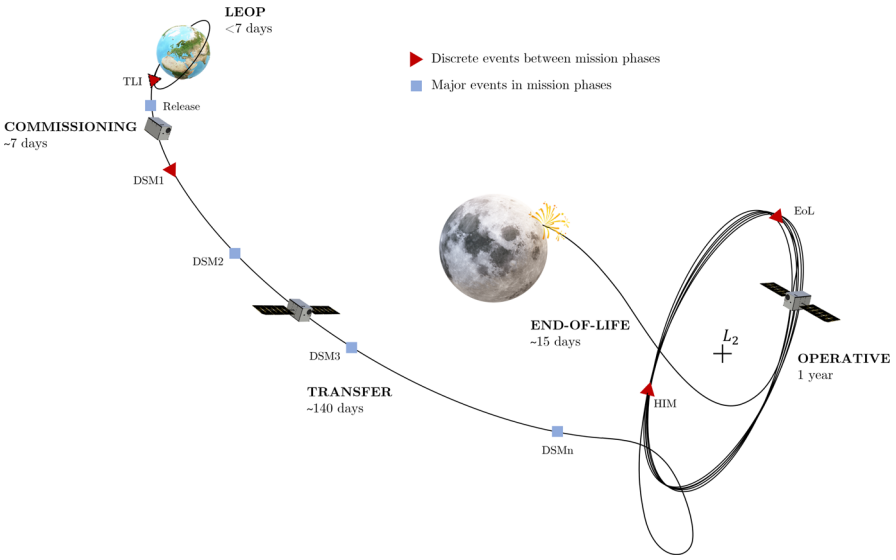


Fig. 2 Sketch of the LUMIO transfer, operational, and disposal trajectories

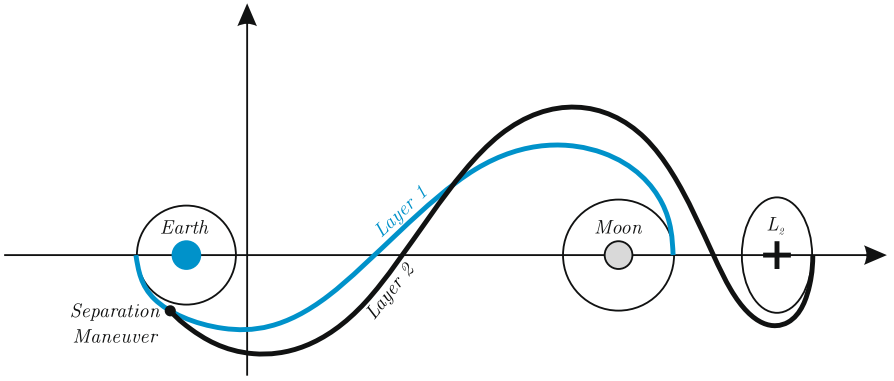


Fig. 3 Two-layers approach for the transfer trajectory

Layer 2 The trajectory followed by LUMIO. After separation from the Layer 1 at the separation maneuver, LUMIO performs its own maneuvers toward the operational quasi-halo orbit.

3.1 Reference Frames and Dynamical Models

The trajectory design is carried out using different dynamical models according to the purpose of each step. Low-energy first guesses are generated in simplified dynamical models, namely the circular restricted three-body problem and the bicircular restricted four-body problem, whereas all final transfer trajectories and quasi-halo orbits are refined in a high-fidelity roto-pulsating restricted n-body problem.

3.1.1 Circular Restricted Three-Body Problem

The circular restricted three-body problem (CR3BP) is adopted as simplified dynamical model to describe the motion of a spacecraft under the gravitational attraction of the Earth and the Moon. In this model, the two primaries are assumed to move on circular orbits about their common barycenter, while the spacecraft is considered massless and does not affect their motion. Although simplified, the CR3BP provides a convenient autonomous framework to compute the ideal Earth–Moon L_2 halo orbit and its invariant manifolds, which are then used as reference objects for the transfer design.

The equations of motion are written in the Earth–Moon synodic frame. This is a uniformly rotating, barycentric, adimensional reference frame whose origin is placed at the Earth–Moon barycenter. The $\hat{\xi}$ axis is directed from the Earth to the Moon, the $\hat{h}$ axis is aligned with the angular momentum of the Earth–Moon motion, and the $\hat{\eta}$ axis completes the right-handed triad. Distances are normalized by the Earth–Moon distance, while time is adimensionalized such that the mean motion of the two primaries is equal to one. In this frame, the Earth and the Moon have fixed positions

$$\boldsymbol{\rho}_E = \begin{bmatrix} -\mu \\ 0 \\ 0 \end{bmatrix}, \qquad \boldsymbol{\rho}_M = \begin{bmatrix} 1-\mu \\ 0 \\ 0 \end{bmatrix}, \tag{1}$$

where

$$\mu = \frac{m_M}{m_E + m_M} \tag{2}$$

is the Earth–Moon mass parameter.

Considering

$$\boldsymbol{\rho} = \begin{bmatrix} \xi \\ \eta \\ \zeta \end{bmatrix} \tag{3}$$

to be the spacecraft position in the synodic frame, the relative position vectors from the spacecraft to the Earth and the Moon are defined as

$$\boldsymbol{\delta}_E = \boldsymbol{\rho} - \boldsymbol{\rho}_E \qquad \boldsymbol{\delta}_M = \boldsymbol{\rho} - \boldsymbol{\rho}_M \tag{4}$$

with magnitudes

$$\delta_E = \sqrt{(\xi+\mu)^2 + \eta^2 + \zeta^2}, \qquad \delta_M = \sqrt{(\xi-1+\mu)^2 + \eta^2 + \zeta^2} \tag{5}$$

The CR3BP equations of motion are [19]

$$\begin{cases} \xi'' - 2\eta' = \frac{\partial \Omega_3}{\partial \xi} \\ \eta'' + 2\xi' = \frac{\partial \Omega_3}{\partial \eta} \\ \zeta'' = \frac{\partial \Omega_3}{\partial \zeta} \end{cases} \tag{6}$$

where primes denote derivatives with respect to the adimensional time and Ω_3 is the three-body pseudo-potential

$$\Omega_3 = \frac{1}{2}\left(\xi^2 + \eta^2\right) + \frac{1-\mu}{\delta_E} + \frac{\mu}{\delta_M} \tag{7}$$

The CR3BP admits the Jacobi integral

$$C_j = 2\Omega_3 - \boldsymbol{\rho}'^T \boldsymbol{\rho}' \tag{8}$$

which is constant along any natural trajectory. In this work, the selected ideal halo orbit around the Earth–Moon L_2 point is characterized by $C_j = 3.09$. Its stable manifold is computed in the CR3BP and used to generate first guesses for the transfer to the operational orbit. The use of the CR3BP for this step is convenient because the model is autonomous; consequently, the invariant manifolds do not depend on the absolute epoch. The final transfer trajectory and the corresponding quasi-halo orbit are then refined in the higher-fidelity dynamics.

3.1.2 Bicircular Restricted Four-Body Problem

The bicircular restricted four-body problem (BC4BP) is adopted to generate low-energy first guesses for the WSB transfer. The model extends the CR3BP by including the gravitational perturbation of the Sun, while retaining an analytical description of the motion of the massive bodies. In particular, the Earth and the Moon are assumed to move on circular orbits around their common barycenter, whereas the Sun moves on a circular orbit around the Earth–Moon barycenter. The spacecraft is assumed to be massless and does not affect the motion of the primaries. Although simplified, the BC4BP captures the dominant solar perturbation responsible for weak-stability-boundary dynamics.

The equations of motion are written in the Earth–Moon synodic frame introduced above. Therefore, the Earth and the Moon have fixed positions

$$\boldsymbol{\rho}_E = \begin{bmatrix} -\mu \\ 0 \\ 0 \end{bmatrix}, \qquad \boldsymbol{\rho}_M = \begin{bmatrix} 1-\mu \\ 0 \\ 0 \end{bmatrix}, \tag{9}$$

where

$$\mu = \frac{m_M}{m_E + m_M} \tag{10}$$

is the Earth–Moon mass parameter. Distances are normalized by the Earth–Moon distance, while time is adimensionalized such that the Earth–Moon mean motion is equal to one.

Considering

$$\boldsymbol{\rho} = \begin{bmatrix} \xi \\ \eta \\ \zeta \end{bmatrix} \tag{11}$$

to be the spacecraft position in the Earth–Moon synodic frame, the Sun position in the same frame is prescribed as

$$\boldsymbol{\rho}_S = a_S \begin{bmatrix} \cos\theta_S \\ \sin\theta_S \\ 0 \end{bmatrix} \tag{12}$$

where a_S is the adimensional Sun–Earth–Moon barycenter distance, expressed in Earth–Moon distance units. The Sun phase evolves as

$$\theta_S(\tau) = \theta_{S,0} + \omega_S \tau \tag{13}$$

where $\theta_{S,0}$ is the initial Sun phase in the Earth–Moon synodic frame and

$$\omega_S = \frac{\omega_{SE}}{\omega_{EM}} - 1 \tag{14}$$

Here, ω_{SE} and ω_{EM} are the Sun–Earth and Earth–Moon mean motions, respectively. Since the Earth–Moon synodic frame rotates with the Earth–Moon system, the Sun appears to move periodically around the Earth–Moon barycenter.

The relative position vectors between the spacecraft and the massive bodies are defined as [20]

$$\boldsymbol{\delta}_j = \boldsymbol{\rho} - \boldsymbol{\rho}_j, \qquad \delta_j = \left\| \boldsymbol{\delta}_j \right\|, \qquad j \in \{E, M, S\}. \tag{15}$$

The BC4BP equations of motion are written as

$$\begin{cases} \xi'' - 2\eta' = \frac{\partial \Omega_{BC}}{\partial \xi} \\ \eta'' + 2\xi' = \frac{\partial \Omega_{BC}}{\partial \eta} \\ \zeta'' = \frac{\partial \Omega_{BC}}{\partial \zeta} \end{cases} \tag{16}$$

where primes denote derivatives with respect to the adimensional time τ. The time-dependent pseudo-potential is

$$\Omega_{BC} = \frac{1}{2}\left(\xi^2 + \eta^2\right) + \frac{1-\mu}{\delta_E} + \frac{\mu}{\delta_M} + \hat{\mu}_S \left(\frac{1}{\delta_S} - \frac{\boldsymbol{\rho}^T \boldsymbol{\rho}_S}{\rho_S^3} \right), \tag{17}$$

with

$$\hat{\mu}_S = \frac{m_S}{m_E + m_M} \tag{18}$$

The last term in Eq. (17) accounts for the direct solar gravitational acceleration and for the indirect acceleration associated with the motion of the Earth–Moon barycenter around the Sun.

Additionally, a Sun–Earth synodic frame can be defined in the BC4BP, hving the center in the Sun–Earth barycenter and the ξ-axis in the Sun-Earth direction. It is useful for visualizing the WSB transfers.

Differently from the CR3BP, the BC4BP is non-autonomous because the Sun position depends explicitly on time through $\theta_S(\tau)$. As a consequence, the Jacobi integral is not conserved. Nevertheless, the model is well suited to generate low-energy WSB trajectories, because it includes the leading-order solar perturbation while preserving a relatively simple dynamical structure. The BC4BP solutions are therefore used only as preliminary guesses and are subsequently refined in a high-fidelity n-body problem.

3.1.3 Roto-Pulsating Restricted *n*-Body Problem

In order to have a high-fidelity dynamics, able to correctly represent the highly nonlinear motion of LUMIO, the roto-pulsating restricted n-body problem (RPRnBP) is exploited [21]. The use of an adimensional roto-pulsating frame eases the motion description both for the transfer trajectory and for the operational orbit, since they are the generalization of trajectory existing in the restricted three-body problem.

Thus, a non-uniformly rotating, barycentric, adimensional reference frame ($\hat{\xi}$, $\hat{\eta}$, $\hat{h}$), called roto-pulsating synodic frame (RPF), is defined in order to write the equation of motion. The center of this system is placed at the primaries barycenter (i.e., Earth–Moon barycenter); the $\hat{\xi}$ axis is aligned with the two primaries, with $\hat{h}$ orthogonal to the plane of motion. Distances are normalized accordingly to the instantaneous distance between the primaries. The unit distance can be defined as

$$k(t) = \|\mathbf{r}_E(t) - \mathbf{r}_M(t)\| \tag{19}$$

where $\mathbf{r}_E$ are $\mathbf{r}_M$ the primaries position in J2000. Therefore, k varies in time according to the mutual position of the two primaries, so creating a pulsating reference system. Moreover, time is adimensionalized such that mean motion about their common barycenter $\omega = \sqrt{\frac{G(m_E+m_M)}{\tilde{a}^3}}$ is set to unity, with (m_E and m_M, the Earth and Moon mass respective and $\tilde{a}$ the mean semi-major axis value. By choosing a constant mean motion, the average primaries revolution period is 2π. In this framework, Earth and the Moon are have fixed position, $[-\mu, 0, 0]^T$ and $[1-\mu, 0, 0]^T$ respectively, with $\mu = m_M/(m_E + m_M)$ being the mass parameter of the system (Fig. 4).

The equations of motion for the RPRnBP reads [22]

$$\boldsymbol{\rho}'' + \frac{1}{\omega}\left(\frac{2\dot{k}}{k}I + 2C^T\dot{C}\right)\boldsymbol{\rho}' + \frac{1}{\omega^2}\left(\frac{\ddot{k}}{k}I + 2\frac{\dot{k}}{k}C^T\dot{C} + C^T\ddot{C}\right)\boldsymbol{\rho} + \frac{C^T\ddot{\mathbf{b}}}{k\omega^2} = \nabla\Omega + \mathbf{a}_{SRP} \tag{20}$$

where $\boldsymbol{\rho}$ is the spacecraft position in the RPF, the primes representing the derivatives with respect to the adimensional time τ, dots indicate the time derivatives and $\nabla\Omega = \partial\Omega/\partial\boldsymbol{\rho}$ is the gradient of the pseudopotential

$$\Omega = \sum_{j\in\mathcal{S}} \frac{\hat{\mu}_j}{\delta_j}\left[1 + \frac{J_{2_j}R_{B_j}^2}{2k^2\delta_j^2}\left(1 - \frac{3\boldsymbol{\delta}_j^T M\boldsymbol{\delta}_j}{\delta_j^2}\right)\right] \tag{21}$$

where $\mathcal{S}$ is the set containing the primaries and characterized by the adimensional gravitational parameter $\hat{\mu}_j = m_j/(m_E + m_M)$, second harmonics coefficient J_{2_j}

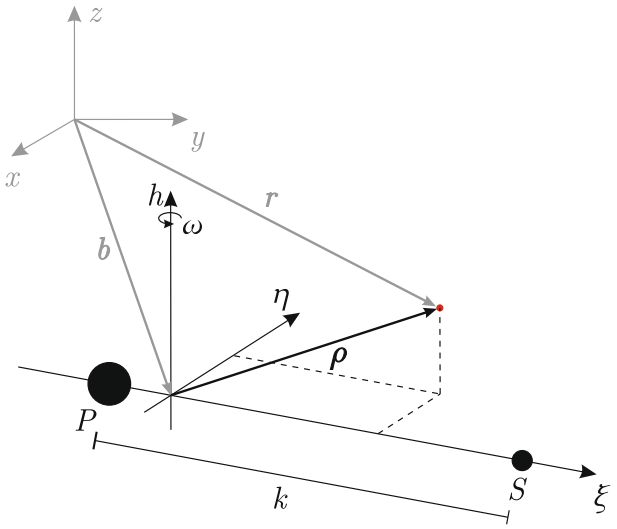


Fig. 4 Rotating, pulsating, non-inertial reference frame. The inertial reference frame and quantities making reference to it are drawn in grey. Spacecraft is the red dot

related to the non-spherical gravitational distribution and equatorial radius R_{B_j}, $M = C^T I_z C$, while $\boldsymbol{\delta}_j = \boldsymbol{\rho} - \boldsymbol{\rho}_j$, and δ_j is its magnitude. The adimensionalized solar radiation pressure (SRP) acceleration in Eq. (20) can be expressed, using the cannon ball model, as

$$\mathbf{a}_{SRP} = \frac{\gamma_0}{\omega^2 k^3} \frac{\boldsymbol{\delta}_S}{\delta_S^3} \tag{22}$$

where $\boldsymbol{\delta}_S$ is the Sun position and γ_0 is the SRP parameter, defined as

$$\gamma_0 = (1 + c_r) \frac{A}{m} \frac{\Psi_0 d_0^2}{c} \tag{23}$$

with c_r the spacecraft reflectivity coefficient, A/m its area-to-mass ratio and c the speed of light in the vacuum.

Mixed derivative notation in Eq. (20) acknowledges that ephemeris data are numeric, discrete, and provided for regular dimensional time. Indeed, planets position $\mathbf{r}_j$ in J2000 are retrieved by using SPICE [23, 24] as well as the physical constants. The transformations from the solar barycentric inertial frame of reference (i.e., J2000) and the RPF are

$$\mathbf{r}(t) = \mathbf{b}(t) + k(t) C(t) \boldsymbol{\rho}(t) \tag{24}$$

$$\mathbf{v}(t) = \dot{\mathbf{b}} + \dot{k} C \boldsymbol{\rho} + k C \omega \boldsymbol{\rho}' \tag{25}$$

$$\tau = \omega (t - t_0) \tag{26}$$

Table 3 Parameters of the dynamics and the spacecraft

Parameter	Symbol	Value
Earth–Moon mass ratio	μ	0.01215058426994
Earth gravitational parameter	μ_E	398,600.4354360959 km^3/s^2
Moon gravitational parameter	μ_M	4902.800066163796 km^3/s^2
Earth mean radius	R_{B_3}	6371.008366666666 km
Moon mean radius	$R_{B_{10}}$	1737.4 km
Earth oblateness coefficient	J_{2_3}	0.001082616
Moon oblateness coefficient	$J_{2_{10}}$	0
SRP parameter	γ_0	2.2106568108×10^6 km^3/s^2
Reflectivity coefficient	c_r	0.08
Area-to-mass ratio	A/m	0.02 m^2/kg
Sun–Earth mean motion	ω_{SE}	1.99099×10^{-7} rad/s
Earth–Moon mean motion	ω_{EM}	2.66170×10^{-6} rad/s

with $\mathbf{b}$ the Earth–Moon barycenter position

$$\mathbf{b}(t) = \frac{m_E \mathbf{r}_E + m_M \mathbf{r}_M}{m_E + m_M} \tag{27}$$

and C the cosine angle matrix between J2000 and the RPF

$$C(t) = [\xi, \eta, h] \tag{28}$$

with

$$\xi = \frac{\mathbf{r}_M - \mathbf{r}_E}{k}, \quad h = \frac{(\mathbf{v}_M - \mathbf{v}_E) \times (\mathbf{r}_M - \mathbf{r}_E)}{\|(\mathbf{v}_M - \mathbf{v}_E) \times (\mathbf{r}_M - \mathbf{r}_E)\|}, \quad \eta = h \times \xi \tag{29}$$

In Table 3, values for the most useful parameters in the dynamics are presented.

3.2 Layer 1

For the Layer 1, it is assumed that the launcher is placed on a circular LEO having an altitude of 200 km, while the target orbit is a circular LLO with an altitude of 100 km. All the other keplerian parameters of both the orbits are considered free to vary. No other nominal maneuver is considered for this layer trajectory, apart from the trans-lunar injection (TLI) and the injection maneuver into the LLO (Fig. 5). The Layer 1 problem can be summarized as:

Problem 1 *(Layer 1 Problem)* Find the departure time t_0, the final time t_f, and the maneuvers $\boldsymbol{\Delta v}_1$ and $\boldsymbol{\Delta v}_2$ such that

$$J = \|\boldsymbol{\Delta v}_1\| + \|\boldsymbol{\Delta v}_2\| \tag{30}$$

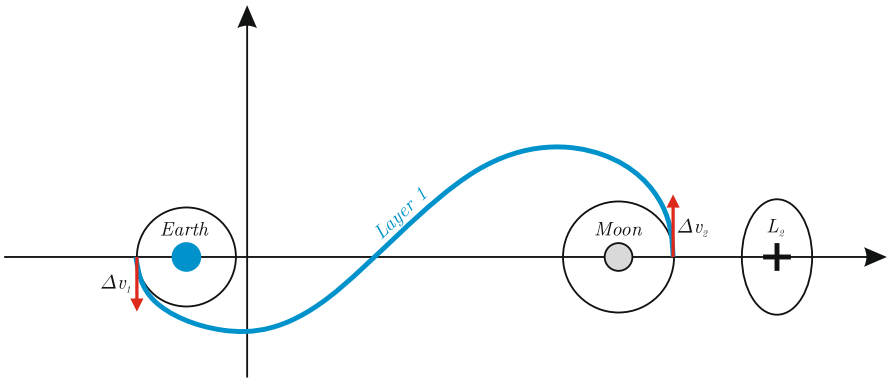


Fig. 5 Schematics for the Layer 1 of the transfer trajectory

is minimized, subjected to the boundary constraints

$$\begin{cases} \|\mathbf{r}(t_0) - \mathbf{r}_E(t_0)\| - R_E & = & 200\,\text{km} & \text{(31a)} \\ (\mathbf{v}(t_0) - \mathbf{v}_E(t_0)) \cdot (\mathbf{r}(t_0) - \mathbf{r}_E(t_0)) & = & 0 & \text{(31b)} \end{cases}$$

and

$$\begin{cases} \|\mathbf{r}(t_f) - \mathbf{r}_M(t_f)\| - R_M & = & 100\,\text{km} & \text{(32a)} \\ \left(\mathbf{v}(t_f) - \mathbf{v}_M(t_f)\right) \cdot \left(\mathbf{r}(t_f) - \mathbf{r}_M(t_f)\right) & = & 0 \quad , & \text{(32b)} \\ \mathcal{E}\left(\mathbf{r}(t_f), \mathbf{v}(t_f) + \boldsymbol{\Delta v}_2\right) & = & 0 & \text{(32c)} \end{cases}$$

where $\mathbf{r}_E$, $\mathbf{v}_E$, $\mathbf{r}_M$, and $\mathbf{v}_M$ denote the position and velocity of the Earth and the Moon, respectively, R_E and R_M are their radius, $\mathcal{E}$ is a map computing the Keplerian eccentricity, and

$$\begin{bmatrix} \mathbf{r}(t_f) \\ \mathbf{v}(t_f) \end{bmatrix} = \varphi\left(\begin{bmatrix} \mathbf{r}(t_0) \\ \mathbf{v}(t_0) + \boldsymbol{\Delta v}_1 \end{bmatrix},\ t_0;\ t_f\right), \tag{33}$$

with φ indicating the integration flow.

Following the methodology in [25], two low-energy transfers are first generated in the BCR4BP. Then, they are refined in the high-fidelity RPRnBP introduced in Sect. 3.1. These solutions are then used as first guesses for Problem 1.

Problem 1 is translated into nonlinear programming problem (NLP) by means of a multiple shooting technique, following the methodology in [21], and then solved using an active-set algorithm.

3.3 Layer 2

Layer 2 represents the trajectory actually followed by LUMIO after release from the mothercraft. The spacecraft is assumed to be deployed 12 h after the TLI, with a release velocity of 1.4 m/s provided by the deployer. The first maneuver of Layer 2 is performed 7 d after the TLI and is denoted as separation maneuver (SM). Although

referred to as separation maneuver, this impulse does not correspond to the physical deployment of LUMIO, which has already occurred 6.5 d earlier. Rather, it marks the dynamical separation between the mothercraft trajectory, associated with Layer 1, and the independent LUMIO transfer trajectory, associated with Layer 2. After the SM, up to seven additional deep-space maneuvers (DSMs) are included to guide LUMIO toward the target halo orbit.The maximum number of DSMs was selected based on preliminary numerical experiments, which showed that no more than five DSMs were generally required to obtain feasible transfers. Two extra maneuver points were therefore introduced to provide additional flexibility and improve the robustness of the optimization process. This choice was later confirmed a posteriori, since the optimized solutions typically required fewer than the maximum number of available maneuvers. A final halo insertion maneuver (HIM) inserts LUMIO in the operational orbit (Fig. 6). Hence, the Layer 2 problem can be summarized as:

Problem 2 *(Layer 2 Problem)* Find the final time t_f, the maneuvers, and their application time, such that

$$J = \|\boldsymbol{\Delta} v_{SM}\| + \|\boldsymbol{\Delta} v_{HIM}\| + \sum_{i=2}^{8} \|\boldsymbol{\Delta} v_i\| \tag{34}$$

is minimized, subjected to the boundaries constraints

$$\begin{cases} \mathbf{r}(t_R) - \mathbf{r}_R = \mathbf{0} & \text{(35a)} \\ \mathbf{v}(t_R) - \mathbf{v}_R = \Delta\mathbf{v}_R, & \text{(35b)} \end{cases}$$

where $\mathbf{r}_R$ and $\mathbf{v}_R$ is the position and velocity at the release, respectively, and $\Delta\mathbf{v}_R$ is the release impulse, and

$$\mathbf{r}(t_f) - \mathbf{r}_{qh}(t_f) = \mathbf{0}, \tag{36}$$

where $\mathbf{r}_{qh}(t_f)$ is the position at the HIM on the quasi-halo.

In order to solve Problem 2, a multiple shooting technique is used to obtain an NLP, following also in this case the methodology in [21], and then solved using an active-set algorithm.

However, infinite quasi-halos can be generated from the CR3BP halo with $C_j = 3.09$. In fact, a different quasi-halo can be generated by changing the epoch at the x–y plane crossing [26]. In order to overcome this issue, a large number of quasi-halos can be produced and then Problem 2 can be solved multiple times using them as final target (see [26], for example). In this case, a large number of optimization should be run, requiring a huge time and computational effort. For this reason, an alternative approach has been devised and it has been illustrated in Fig. 7.

The proposed strategy solves Problem 2 through a three-step procedure:

1. Problem 2 is first solved by targeting the ideal CR3BP halo orbit, while propagating the transfer trajectory in the high-fidelity RPRnBP. At this stage, no dynamical continuity is imposed between the transfer and the final orbit. Therefore, a specific quasi-halo orbit does not need to be defined in advance.

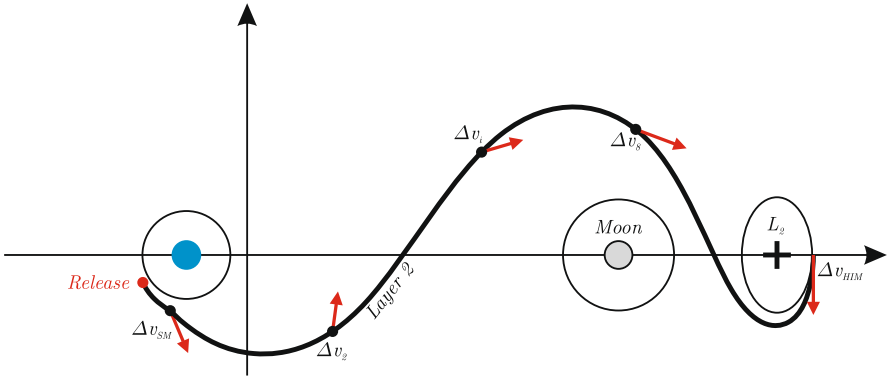


Fig. 6 Schematics for the Layer 2 of the transfer trajectory

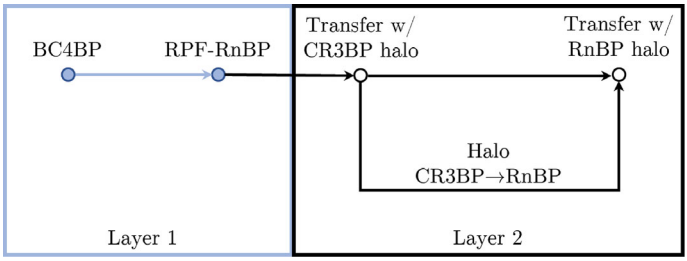


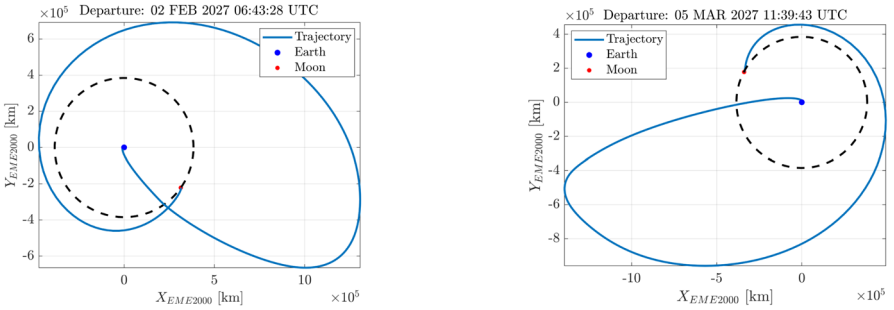
Fig. 7 Scheme for the Layer 1 and Layer 2 problem solution

2. A quasi-halo orbit is then generated in the RPRnBP starting from the final target point identified on the CR3BP halo in Step 1. This choice reduces the initial state mismatch at the HIM point, thereby easing the subsequent targeting in the higher-fidelity model.
3. Finally, Problem 2 is solved again by replacing the ideal CR3BP halo with the quasi-halo generated in Step 2. The transfer obtained in Step 1 is used as the initial guess for this final refinement.

4 Results

4.1 Layer 1

In order to compute the trajectories related to Layer 1, following the scheme in Fig. 7, two first guesses are computed in the BC4BP. The choice of having two first guesses is related to the fact that it is known that two kind of WSB transfer classes exists, one having their apogee in the II quadrant of the Sun–Earth synodic frame, and the other in IV quadrant [27]. First guesses are shown in Fig. 8, while initial conditions are reported in Table 4. The initial conditions have been randomly selected from the database in [25].



(a) II quadrant (b) IV quadrant

Fig. 8 First guesses for the Layer 1 optimization problem depicted in J2000

Table 4 Initial conditions for the first guesses of Layer 1. Values are in the adimensional Earth–Moon synodic frame

Type	ρ [-]	ρ' [-]	τ [-]
II quadrant	[−0.001131604619028	[−8.174722278049826	6.237035398286292
	0.012979814458067	6.939836131487377	
	0]	0]	
IV quadrant	[−0.025801912216061	[6.401371275095031	4.875637208835165
	−0.025801912216061	−8.588028885753099	
	0]	0]	

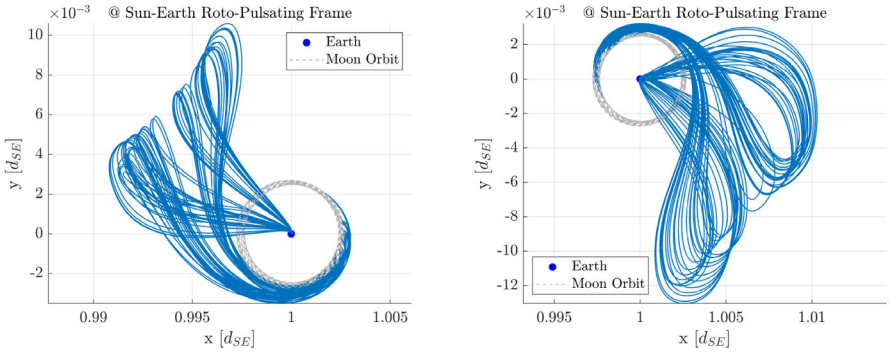
Next, Problem 1 is solvedby seeking one trajectory per synodic month throughout 2027 (about every 29.53 days), consistent with the synodic periodicity of the BC4BP primary configuration. This sampling both generates a diverse solution set and allows any epoch-dependent effects to be identified. The resulting optimized trajectories are shown in Fig. 9. All the solutions require a total cost of about 3.850 km/s, while the time of flight varies from 115 to 130 days (Fig. 10).

4.2 From Layer 1 to Layer 2

Layer 1 trajectory cannot be used directly as an initial guess for the Layer 2 optimization, since Problems 1 and 2 have different target conditions. A dedicated first-guess generation procedure is therefore introduced. This procedure combines the Layer 1 trajectory, the release conditions, and the stable manifold of the ideal CR3BP target halo orbit to construct dynamically meaningful initial guesses for the transfer to the operational orbit.

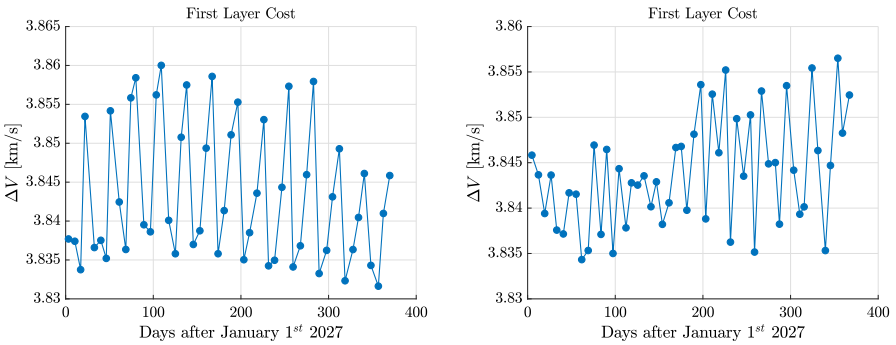
The procedure consists of two main steps:

1. A search-space analysis is first performed at release. Several post-release trajectories are propagated forward from different release directions, and the most promising candidates are selected according to their potential proximity to the halo stable manifolds.



(a) II quadrant transfers. (b) IV quadrant transfers.

Fig. 9 First layer solutions for each week. Distances are in astronomical units d_{SE}



(a) II quadrant cost. (b) IV quadrant cost.

Fig. 10 First layer Δv for each week

2. The selected post-release trajectories are then further filtered using criteria based on their distance from the Moon and their orbital energy. Intersections between these trajectories and backward-propagated stable manifolds of the CR3BP halo are finally used to construct the Layer 2 initial guesses.

4.2.1 Release Direction Analysis

In order to identify possible favorable release directions, a sensitivity analysis is performed. All the possible release conditions are simulated, by defining a sphere of 1000 uniform distributed points and with radius equal to the release velocity Δv_R, i.e., the 1.4 m/s-impulse given by the deployer to the CubeSat at the release, for each first layer solution. The sphere is centered at the release point $\mathbf{r}_R$, and the release (relative) velocity $\Delta \mathbf{v}_R$ is applied to the carrier spacecraft velocity to obtain LUMIO's state immediately after release:

$$\mathbf{x}(t_R) = \mathbf{x}_R + \begin{bmatrix} \mathbf{0} \\ \Delta \mathbf{v}_R \end{bmatrix} = \begin{bmatrix} \mathbf{r}_R \\ \mathbf{v}_R \end{bmatrix} + \begin{bmatrix} \mathbf{0} \\ \Delta \mathbf{v}_R \end{bmatrix} = \begin{bmatrix} \mathbf{r}(t_R) \\ \mathbf{v}(t_R) \end{bmatrix}. \tag{37}$$

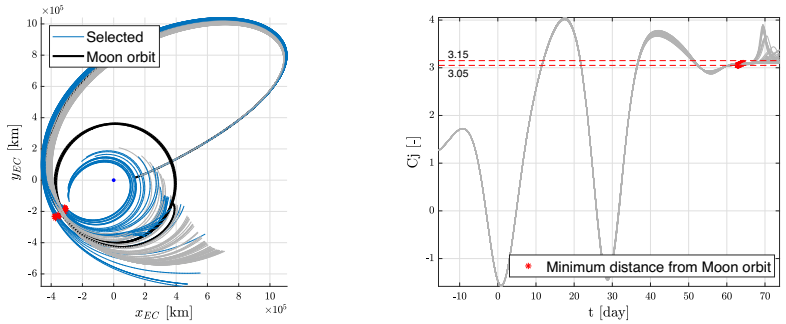
All the 1000 initial states are propagated forward, and then filtered according to the following criteria:

- **Geometric similarity**: The geometric similarity between post–release and Layer 1 trajectories has been assessed exploiting the Pearson correlation coefficient [28], that is a measure of linear correlation between two sets of data, in this case the position related to post-release and Layer 1 trajectories. It is defined as

$$r = \frac{\sum_i \left(\tilde{\xi}_i - \xi_i\right)\left(\tilde{\eta}_i - \eta_i\right)\left(\tilde{\zeta}_i - \zeta_i\right)}{\sqrt{\sum_i \left(\tilde{\xi}_i - \xi_i\right)^2}\sqrt{\sum_i \left(\tilde{\eta}_i - \eta_i\right)^2}\sqrt{\sum_i \left(\tilde{\zeta}_i - \zeta_i\right)^2}} \tag{38}$$

  where the tilde indicates the post-release trajectory while plain variables are associated to the Layer 1 states. Trajectories with a Pearson correlation coefficient with the nominal Layer 1 trajectory higher than 0.65 are selected.
- **Jacobi constant**: The Jacobi constant C_j is the most important parameter because, in the ideal case, a Jacobi constant equal to 3.09 would mean a cheap or free insertion in the halo orbit. The Jacobi energy in the ephemeris model is not constant and evolves in time, but one point is selected to choose the most suitable trajectories. Specifically, this point is defined as the intersection between the post-release trajectory and a reference plane. This plane is perpendicular to the ecliptic and contains the spacecraft velocity vector at the beginning of the transfer phase, before the lunar-orbit crossing. The choice of this reference point is an algorithmic design choice. Preliminary numerical tests showed that evaluating C_j too close to the release epoch provides limited discrimination, since the post-release trajectories are still close to the Layer 1 solution. Conversely, evaluating it too late in the transfer tends to be overly restrictive and may discard trajectories that could still lead to useful manifold intersections. The selected point was therefore chosen as a compromise: it is sufficiently far from release for the different post-release trajectories to have separated dynamically, while still preceding the final lunar-region evolution where the filtering would become too sensitive to the specific phasing of the trajectory. No formal optimality is claimed for this point; rather, it was selected empirically as the location that provided the most effective balance between retaining a sufficiently rich set of candidate trajectories and removing clearly unsuitable ones. Once the Jacobi constant is computed at this intersection point, only trajectories whose Jacobi constant is in the interval [3.05, 3.15] are selected.
- **Moon distance**: The same intersection point is used to determine the relative distance to the lunar orbital radius. In particular, trajectories whose distance is higher than 100,000 km are filtered out. This choice has been made since the operational halo orbit is at a distance between 40,000 km and 80,000 km from the Moon.

In summary, the set of trajectories is initially filtered based on geometric similarity to the Layer 1 trajectory. Subsequently, a reference point is defined to facilitate the selection of the most suitable trajectories. At this point, the Jacobi constant and the



(a) Set of post-release trajectories in the Earth-centered J2000 reference frame.

(b) C_j evolution along a subset of post-release trajectories.

Fig. 11 Results of the sensitivity analysis on the release condition for a single Layer 1 trajectory

distance from the Moon are computed to identify the optimal trajectories for further analysis. The set of trajectories arising from this analysis, along with the C_j evolution of the selected ones are shown in Fig. 11 for a Layer 1 trajectory.

4.2.2 First Guesses Generation

Once the search-space analysis on the release conditions is complete, it becomes essential to narrow down the search field to a small set of candidate trajectories, to limit the computational effort. For this reason, the following selection criteria are considered to further skim the search space:

- ΔC_j, that is the difference between the mean Jacobi constant, across the final part of the transfer, and the Jacobi constant of the ideal halo (3.09).
- Δ_M, that is the mean distance to the Moon, across the final part of the transfer.

These criteria are motivated by the expectation that trajectories with a close lunar approach and a Jacobi constant near that of the nominal halo orbit are more likely to lie near the stable manifold of the target orbit, thereby lowering the Δv required for the HIM. The best trajectory is chosen according to the minimization of both criteria. This is achieved by finding the minimum of the sum of the squares

$$\min_i \quad S_i = (\Delta C_j)_i^2 + (\Delta_M)_i^2 \quad \text{for } i = 1, \ldots, N_t, \tag{39}$$

where N_t is the number of good trajectories resulting from the sensitivity analysis, for each Layer 1 solution. This corresponds to finding the minimum distance from the origin in the $(\Delta_M, \Delta C_j)$ plane, as it can be seen in Fig. 12.

After the selection of the post-release trajectory, intersections are sought between its forward propagation and the backward propagation of the stable manifold of the ideal halo. A schematic representation of the first guess generation strategy can be seen in Fig. 13. Both propagations are done in the synodic Earth–Moon reference frame: the forward propagation is done with the complete dynamical model of the RPRnBP,

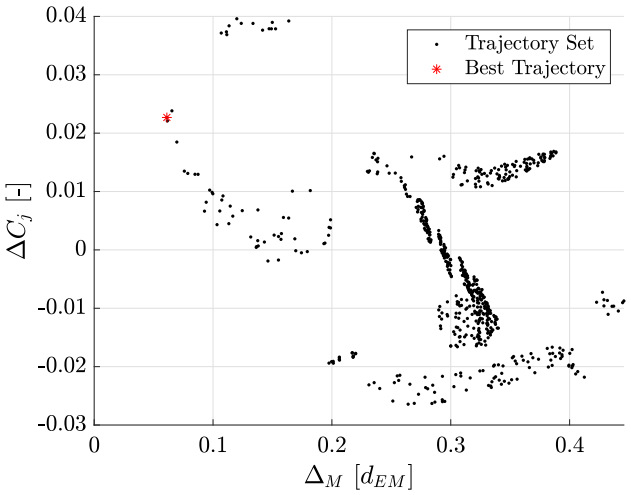


Fig. 12 Post–release trajectory selection: Each dot represent a post–release trajectory associated with a single Layer 1 solution. The red star marks the trajectory closest to the origin, which is therefore selected. The axes use different scales to improve readability. Δ_M is measured in Earth–Moon distance units

while the backward propagation relies on the simplified model of the CR3BP. The choice to adopt the simplified model for the stable manifold is due to the fact that this model is autonomous, so it does not depend on the epoch as it is for the complete model. This allows to search for a higher number of intersections, because the time on the trajectory and the propagation time on the manifold are not correlated. Therefore, the intersection search is performed over three independent parameters:

- the dimensional epoch on the forward-propagated post-release trajectory, measured from the TLI epoch;
- the backward CR3BP propagation time along the stable manifold, measured from the selected halo state to the manifold point;
- the halo phase, defined as the normalized time along one period of the CR3BP halo orbit.

The intersection are, then, ranked by the closest distance in terms of position and velocity. The set of the 10 closest intersections defines the first guesses used to solve Problem 2. An example of a first guess created with this strategy can be seen in Fig. 14, where also the difference between the corresponding Layer 1 trajectory can be appreciated.

4.3 Layer 2

The first step of Layer 2, which considers the CR3BP halo as target orbit, is solved using the 10 best-ranked first guesses for each solution of the Layer 1, i.e., for each week of 2027. This creates a total of 1040 different solutions, which are reduced to one per week for both quadrants by considering the minimum Δv, so that 104 trajectories are the output for the first step of Layer 2. The best solution found for each week is

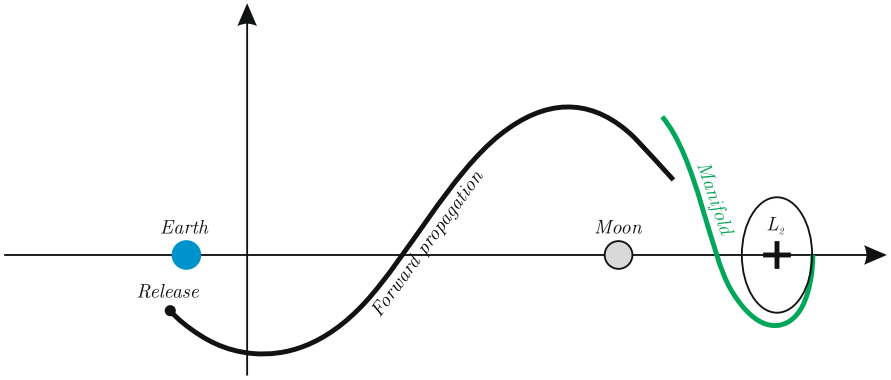


Fig. 13 First guess generation schematics

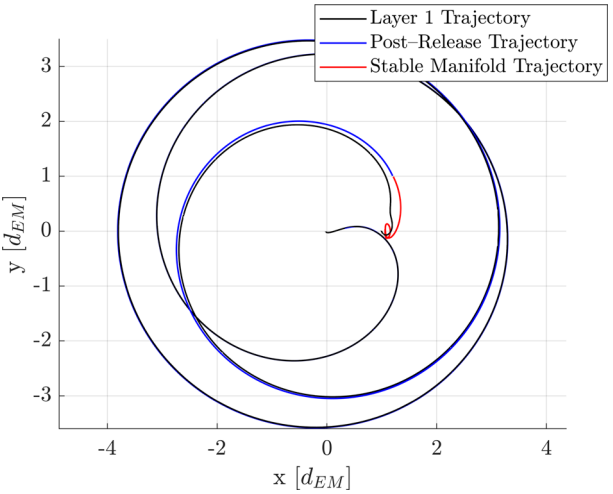


Fig. 14 Example of a first guess trajectory plotted in the Earth–Moon synodic frame

carried forward to Step 2, where it is re-optimized in the high-fidelity RPRnBP model, yielding one optimized trajectory per week in 2027.

In the second step, the target quasi-halo is obtained exploiting the methodology illustrated in [29]. A multiple shooting algorithm is used to impose the continuity of the quasi-halo in the RPRnBP, minimizing an objective function that depends only on the continuity constraints. In addition to the methodology of [29], constraints regarding the difference between the state on the ideal halo and on the quasi-halo at the epoch of the HIM are imposed

$$\begin{cases} \|\mathbf{r}_h(t_f) - \mathbf{r}_{qh}(t_f)\| & \leq & 300\,\text{km} & \text{(40a)} \\ \|\mathbf{v}_h(t_f) - \mathbf{v}_{qh}(t_f)\| & \leq & 0.01\,\text{km/s} & \text{(40b)} \end{cases}$$

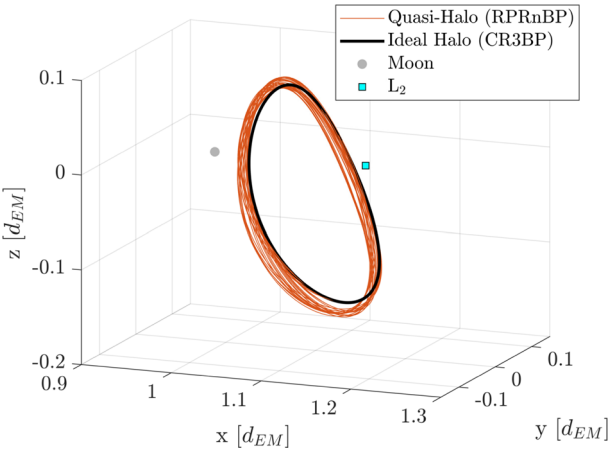


Fig. 15 Quasi-halo and ideal halo trajectories in the roto-pulsating reference frame

where $\mathbf{r}_h$, $\mathbf{v}_h$, $\mathbf{r}_{qh}$, and $\mathbf{v}_{qh}$ are the position and velocity vectors on the halo and quasi-halo, respectively, and t_f is the final time of the transfer. These constraints allow to compute a quasi-halo with insertion states similar to the one of the ideal halo, preserving both a similar HIM and total cost. An example of the results of the second step computations can be seen in Fig. 15, where the trajectory of a quasi-halo can be compared to the ideal halo.

Finally, transfers are refined to target the quasi-halo, solving Problem 2 for each of the 52 solutions. In Fig. 16 the total Δv needed for each week of the year is shown. From the figure it is possible to see an annual trend: the average cost indeed oscillates over 40 m/s, even though the weekly variations are relevant. This is due to the variability of the first layer, whose trajectories differ considerably between each other (as per Fig. 9). The more the final part of the trajectory of the first layer is distant from the stable manifold of the target orbit, the higher is the cost of the transfer, as the insertion in the stable manifold. An analysis on the impact of the Layer 1 trajectory on the Layer 2 transfer cost is reported in Sect. 4.4. Maximum, minimum, and average properties of the 52 optimal transfers are shown in Table 5. It can be noted that in every case the maximum number of DSM (8) is unnecessary, as on average LUMIO will need only 2 DSM to complete the transfer. Moreover, in each trajectory the cost of the HIM is under 1 m/s, which means that the DSMs are able to correctly inject LUMIO on the stable manifold of the quasi-halo. This is preferable both for the total cost, which proves the goodness of the first guess and subsequent optimization, and both for the safety of the transfer, as a trajectory injected in the stable manifold should remain close to the target orbit even if the HIM is not performed at the nominal epoch.

The trajectory associated with the week 20 of 2027, which departs on May 19, 2027, is chosen as an example of the LUMIO transfer orbit. The trajectory can be seen in Fig. 17 and information about the maneuvers is reported in Table 6. It can be noted that the transfer requires only 2 DSMs, DSM-3 and DSM-4, which are located around the apogee, so minimizing their cost. After the DSM-4, performed 44.85 days after

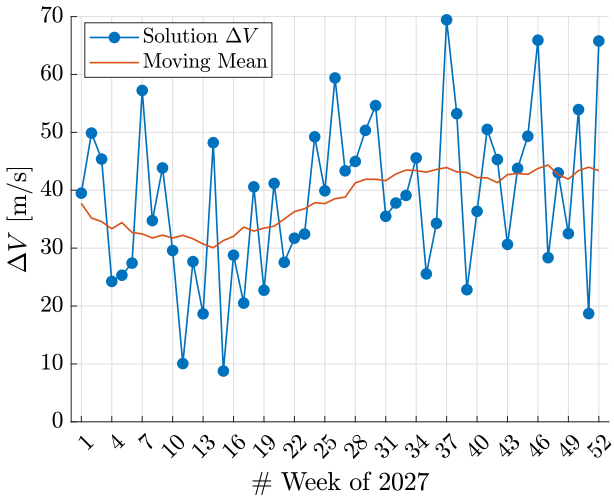


Fig. 16 Transfer Δv for Layer 2 solutions. Each dot represents the best solution for each week and for both quadrants. The orange line represents the moving mean to highlight the annual variability of the cost

Table 5 Layer 2 properties

	Δv (m/s)	ToF (d)	Apogee (km)	# DSM (-)	Δv_{HIM} (m/s)
Max	69.44	149.06	1.972×10^6	5	0.97
Min	8.77	96.04	1.347×10^6	1	0
Mean	38.56	117.71	1.527×10^6	2	0.23

the TLI, LUMIO will follow the stable manifold for $\sim 50\,d$, until the small insertion maneuver on the quasi-halo.

4.4 Impact of Layer 1 on Layer 2 Cost

As anticipated, the Layer 2 transfer cost is strongly affected by the specific Layer 1 trajectory used as departure backbone. This dependency is expected because the release state determines the geometry, energy level, and phasing of the subsequent post-release trajectory with respect to the stable manifold of the target halo orbit. As a matter of fact, the dynamical distance of the Layer 1 trajectory from the stable manifold of the target halo orbit plays a dominant role: the farther the trajectory is from the manifold, the higher the cost required for the corresponding Layer 2 transfer. To better illustrate this, an analysis on the impact of Layer 1 on Layer 2 cost is performed. This analysis is intended to provide an illustrative sensitivity case, rather than a complete statistical characterization of the dependence of Layer 2 cost on the TLI state. Specifically, the following cases are considered:

- What happens to Layer 2 if a different Layer 1 is computed in a similar departure epoch

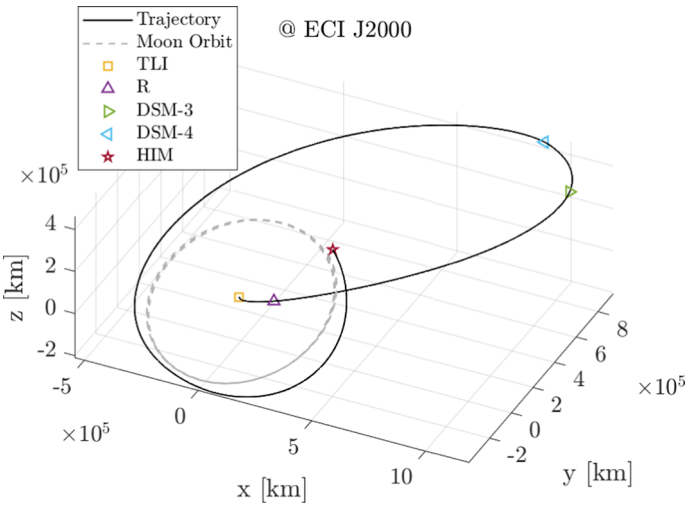


Fig. 17 Baseline transfer trajectory in Earth-centered J2000

Table 6 Maneuvers of the baseline transfer trajectory

	Epoch (UTC)	Time after t_0 (d)	Δv (m/s)
TLI	19 MAY 2027 02:10:04	0	–
R	19 MAY 2027 14:10:04	0.5	–
DSM-1	26 MAY 2027 02:10:04	7.00	0
DSM-2	08 JUN 2027 02:58:23	20.03	0
DSM-3	17 JUN 2027 15:13:04	29.54	7.22
DSM-4	02 JUL 2027 22:29:25	44.85	33.63
DSM-5	12 JUL 2027 20:19:43	54.76	0
DSM-6	19 JUL 2027 12:54:26	61.45	0
DSM-7	08 AUG 2027 14:44:10	81.52	0
DSM-8	13 AUG 2027 23:30:44	86.89	0
HIM	24 AUG 2027 03:07:20	97.04	0.32
Total		97.04	41.18

- What happens if Layer 1 is bypassed by using a dedicated launch for LUMIO

To address the first point, as an example, a completely new Layer 1 is recomputed together with the correlated Layer 2 for week 45 of 2027, by changing the TLI time by 12 h. Table 7 displays the results. The comparison shows that a relatively small change in the TLI epoch, and therefore in the resulting Layer 1 trajectory, may lead to a significant variation of the Layer 2 cost. This suggests that the exact TLI state can play an important role in determining the cost of the LUMIO transfer.

Regarding the second point, dedicated launches are computed for 2 of the 52 weeks. This is achieved by using the Layer 2 trajectory as the first guess and by imposing the initial conditions of Problem 1 (i.e., launch on a LEO) and the final conditions of

Table 7 Effect of Layer 1 change on Layer 2

Week 45	TLI Epoch (UTC)	Layer 2 Δv (m/s)
Original	12 NOV 2027 12:26:54	49.33
New	13 NOV 2027 02:44:52	33.16

Table 8 Comparison between shared and dedicated launch

2027 Week	Transfer Δv (m/s)	
	Shared launch	Dedicated launch
20	41.18	10.62
37	69.44	5.48

Problem 2 (i.e., arrival on the quasi-halo orbit). Results are reported in Table 8, where it can be seen that, as expected, a big reduction in cost is possible if a dedicated launch is used. Additionally, if a first guess generation strategy and optimization problem is tailored for this dedicated launch scenario, better results can be achieved, showing that completely ballistic WSB transfers to the quasi-halo are possible in this case [30]. Further examples of dedicated-launch WSB transfers to libration-point orbits, including cases tailored directly to the final operational orbit, are reported in [30].

The analyses performed suggest that the impact of the Layer 1 on the Layer 2 cost is high. As a consequence, at the moment is not possible to give precise launch windows for LUMIO. Once a launcher is selected, and the range of possible TLI states is characterized, which ultimately defines the potential first layers, then the variability of the transfer cost for LUMIO will be reduced. This will allow to study the relevance of the departure epoch on the transfer cost and, in turn, define launch window opportunities for the mission.

5 Conclusions

This work presented the transfer trajectory design and analysis of LUMIO performed during Phase B. The possibility to exploit weak stability boundaries to reach the operational halo orbit has been investigated, and selected as baseline scenario. The increasing use of low-energy lunar transfers, combined with the availability of a cost-effective dedicated launch, expands LUMIO rideshare options. Most importantly, the WSB trajectory cuts the required Δv from 120 m/s (for the Phase 0 low-lunar-orbit release) to under 70 m/s. This reduction shrinks the propellant-tank volume, freeing up internal space for other subsystems. Additionally, this new approach yields also longer commissioning windows and less demanding flight dynamics operations.

Acknowledgements This journal article extends our earlier conference paper [31] with additional results and offers a more comprehensive analysis of the outcomes.

Author Contributions C.G.: conceptualization, methodology, software, formal analysis, writing—original draft, visualization. A.M.: methodology, software, formal analysis, writing—review and editing, visualization. C.B.: methodology, software, formal analysis, writing—review and editing, visualization. G.M.: conceptualization, writing—review and editing, supervision. V.F.: conceptualization, writing—review and

editing, supervision. F.T.: conceptualization, writing—review and editing, supervision, project administration.

Funding Open access funding provided by Politecnico di Milano within the CRUI-CARE Agreement. The work described in this paper is part of LUMIO Phase B study, which has been funded by the European Space Agency (ESA) under the General Support Technology Programme (GSTP), ESA contract No. 4000139301/22/NL/AS. LUMIO Phase B has been supported by the national delegations of Italy (ASI) and Norway (NOSA). The authors would like to acknowledge the LUMIO Team, including ESA's experts.

Data Availability The dataset generated in this study is available at https://doi.org/10.5281/zenodo.15172935. The dataset contains also the SPICE kernel of the transfer depicted in Fig. 17 and its associated operational orbit.

Declarations

Conflict of interest The authors have no conflict of interest to declare that are relevant to the content of this article.

Open Access This article is licensed under a Creative Commons Attribution 4.0 International License, which permits use, sharing, adaptation, distribution and reproduction in any medium or format, as long as you give appropriate credit to the original author(s) and the source, provide a link to the Creative Commons licence, and indicate if changes were made. The images or other third party material in this article are included in the article's Creative Commons licence, unless indicated otherwise in a credit line to the material. If material is not included in the article's Creative Commons licence and your intended use is not permitted by statutory regulation or exceeds the permitted use, you will need to obtain permission directly from the copyright holder. To view a copy of this licence, visit http://creativecommons.org/licenses/by/4.0/.

References

1. Ceplecha, Z., Borovička, J., Elford, W.G., ReVelle, D.O., Hawkes, R.L., Porubčan, V., Šimek, M.: Meteor phenomena and bodies. Space Sci. Rev. **84**(3), 327–471 (1998). https://doi.org/10.1023/A:1005069928850
2. Merisio, G., Topputo, F.: Present-day model of lunar meteoroids and their impact flashes for Lumio mission. Icarus **389**, 115180 (2023). https://doi.org/10.1016/j.icarus.2022.115180
3. Oberst, J., Christou, A., Suggs, R., Moser, D., Daubar, I.J., McEwen, A.S., Burchell, M., Kawamura, T., Hiesinger, H., Wünnemann, K., Wagner, R.V., Robinson, M.S.: The present-day flux of large meteoroids on the lunar surface-A synthesis of models and observational techniques. Planet. Space Sci. **74**(1), 179–193 (2012). https://doi.org/10.1016/j.pss.2012.10.005
4. Bellot Rubio, L.R., Ortiz, J.L., Sada, P.V.: Luminous efficiency in hypervelocity impacts from the 1999 Lunar Leonids. Astrophys. J. Lett. **542**(1), 65–68 (2000). https://doi.org/10.1086/312914
5. Koschny, D., McAuliffe, J.: Estimating the number of impact flashes visible on the Moon from an orbiting camera. Meteorit. Planet. Sci. **44**(12), 1871–1875 (2009). https://doi.org/10.1111/j.1945-5100.2009.tb01996.x
6. Cervone, A., Topputo, F., Speretta, S., Menicucci, A., Turan, E., Di Lizia, P., Massari, M., Franzese, V., Giordano, C., Merisio, G.: LUMIO: a CubeSat for observing and characterizing micro-meteoroid impacts on the lunar far side. Acta Astronaut. **195**, 309–317 (2022). https://doi.org/10.1016/j.actaastro.2022.03.032
7. Topputo, F., Merisio, G., Franzese, V., Giordano, C., Massari, M., Pilato, G., Labate, D., Cervone, A., Speretta, S., Menicucci, A.: Meteoroids detection with the Lumio lunar CubeSat. Icarus **389**, 115213 (2023). https://doi.org/10.1016/j.icarus.2022.115213
8. Franzese, V., Di Lizia, P., Topputo, F.: Autonomous optical navigation for the lunar meteoroid impacts observer. J. Guid. Control. Dyn. **42**(7), 1579–1586 (2019). https://doi.org/10.2514/1.G003999
9. Cipriano, A., Dei Tos, D., Topputo, F.: Orbit design for LUMIO: the lunar meteoroid impacts observer. Front. Astron. Space Sci. **5**, 29 (2018). https://doi.org/10.3389/fspas.2018.00029

10. Giordano, C., Topputo, F.: Analysis, design, and optimization of robust trajectories in cislunar environment for limited-capability spacecraft. J. Astronaut. Sci. **70**(6), 53 (2023). https://doi.org/10.1007/s40295-023-00413-8
11. Muylle, J.L.D.: Transfer trajectory design to Lagrangian points exploiting weak stability boundaries. Master's Thesis, Politecnico di Milano (2022). https://hdl.handle.net/10589/195214
12. Belbruno, E.A., Miller, J.K.: Sun-perturbed earth-to-moon transfers with ballistic capture. J. Guid. Control. Dyn. **16**(4), 770–775 (1993). https://doi.org/10.2514/3.21079
13. Song, Y.-J., Bae, J., Hong, S., Bang, J.: Korea pathfinder lunar orbiter flight dynamics simulation and rehearsal results for its operational readiness checkout. J. Astron. Space Sci. **39**(4), 181–194 (2022). https://doi.org/10.5140/JASS.2022.39.4.181
14. Cheetham, B.: Cislunar autonomous positioning system technology operations and navigation experiment (CAPSTONE). In: ASCEND 2021, p. 4128 (2021)
15. Maltagliati, L.: A long-awaited return to the Moon. Nat. Astron. **7**(1), 10–10 (2023). https://doi.org/10.1038/s41550-022-01877-8
16. Hoffman, A.E.: Design of lunar transfer trajectories for secondary payload missions, Purdue University (Master' Thesis) (2023). https://doi.org/10.25394/PGS.22695991
17. Badiali, J.: Incorporation of lunar passages into secondary payload transfer design, Purdue University (Master' Thesis) (2024). https://doi.org/10.25394/PGS.27932124
18. Cohen, B.A., Hayne, P.O., Greenhagen, B., Paige, D.A., Seybold, C., Baker, J.: Lunar flashlight: illuminating the lunar south pole. IEEE Aerosp. Electron. Syst. Mag. **35**(3), 46–52 (2020). https://doi.org/10.1109/MAES.2019.2950746
19. Szebehely, V.: Theory of Orbits: The Restricted Problem of Three Bodies. Elsevier, London (1967)
20. Simó, C., Gómez, G., Jorba, À., Masdemont, J.: The bicircular model near the triangular libration points of the rtbp. In: From Newton to Chaos: Modern Techniques for Understanding and Coping with Chaos in N-body Dynamical Systems, pp. 343–370 (1995)
21. Dei Tos, D.A., Topputo, F.: High-fidelity trajectory optimization with application to saddle-point transfers. J. Guid. Control. Dyn. **42**(6), 1343–1352 (2019). https://doi.org/10.2514/1.G003838
22. Dei Tos, D.A., Topputo, F.: Trajectory refinement of three-body orbits in the real solar system model. Adv. Space Res. **59**(8), 2117–2132 (2017). https://doi.org/10.1016/j.asr.2017.01.039
23. Acton, C.H., Jr.: Ancillary data services of NASA's navigation and ancillary information facility. Planet. Space Sci. **44**(1), 65–70 (1996). https://doi.org/10.1016/0032-0633(95)00107-7
24. Acton, C., Bachman, N., Semenov, B., Wright, E.: A look towards the future in the handling of space science mission geometry. Planet. Space Sci. **150**, 9–12 (2018). https://doi.org/10.1016/j.pss.2017.02.013
25. Oshima, K., Topputo, F., Yanao, T.: Low-energy transfers to the Moon with long transfer time. Celest. Mech. Dyn. Astron. **131**, 1–19 (2019). https://doi.org/10.1007/s10569-019-9883-7
26. Oguri, K., Oshima, K., Campagnola, S., Kakihara, K., Ozaki, N., Baresi, N., Kawakatsu, Y., Funase, R.: EQUULEUS trajectory design. J. Astronaut. Sci. **67**(3), 950–976 (2020). https://doi.org/10.1007/s40295-019-00206-y
27. Circi, C., Teofilatto, P.: On the dynamics of weak stability boundary lunar transfers. Celest. Mech. Dyn. Astron. **79**, 41–72 (2001). https://doi.org/10.1023/A:1011153610564
28. Fisher, R.A.: Statistical methods for research workers. In: Breakthroughs in Statistics: Methodology and Distribution, pp. 66–70 (1970). https://doi.org/10.1007/978-1-4612-4380-9_6
29. Dei Tos, D.A., Topputo, F.: Trajectory refinement of three-body orbits in the real solar system model. Adv. Space Res. **59**(8), 2117–2132 (2017). https://doi.org/10.1016/j.asr.2017.01.039
30. Martinelli, A., Buonagura, C., Giordano, C., Topputo, F.: Design and optimisation of weak stability boundary transfers to unstable libration-point orbits: an application to the lumio cubesat. In: 29th International Symposium on Space Flight Dynamics (ISSFD), pp. 1–8 (2024)
31. Giordano, C., Buonagura, C., Martinelli, A., Merisio, G., Franzese, V., Topputo, F.: Trajectory design and analysis of the lumio cubesat. In: AIAA Scitech 2024 Forum, 1271 (2024). https://doi.org/10.2514/6.2024-1271

Publisher's Note Springer Nature remains neutral with regard to jurisdictional claims in published maps and institutional affiliations.